Proceedings World Geothermal Congress 2020+1
Reykjavik, Iceland, April - October 2021

Geothermal Reservoir Characterization and Monitoring through Seismic (Ambient Noise) And Geodetic (InSAR) Imaging applied on Torfajökull Volcano and Reykjanes Peninsula, Iceland.

Joana E. MARTINS[1,2], Andrew HOOPER[3], Ramon F. HANSSEN[2]

TNO, Princetonlaan 6 3584 CB Utrecht

Department of Geoscience and Remote Sensing, Delft University of Technology, the Netherlands

School of Earth and Environment, University of Leeds

Joana.estevesmartins@tno.nl

Keywords: Seismic Imaging, Geodetic Imaging, Reservoir Characterization, Torfajökull volcano, Reykjanes Peninsula, High Enthalpy Geothermal

ABSTRACT

After decades of oil, gas, and coal exploitation, we have learned about some of the unpleasant aftereffects of subsurface resource exploration. Adverse long-term impacts, some known during exploration periods, others only afterwards, may include induced seismicity, land subsidence, or even sinkholes. While geothermal is currently seen as a sustainable source of energy, seismicity induced by inappropriate operational procedures or lack of knowledge of the subsurface may incite doubt and public sensitivity about its future use. A problem frequently posed before and during geothermal exploration is the cost of geophysical measurements for resource assessment, subsurface characterization during the prospection phase, and monitoring accompanying production.

In this study, we investigate and discuss the potential of two economic geophysical measurement techniques for geothermal reservoir characterization and monitoring: passive seismic interferometry for better subsurface characterization through seismic imaging (static model), and satellite-based radar interferometry for geodetic imaging (dynamic model). Seismic imaging using passive seismic techniques allows for subsurface characterization via Ambient Noise Tomography, and supports the assessment of geothermal resources without requiring the use of shooting, which reduces the cost compared to active seismics. Geodetic imaging, by measuring the surface displacements during and after production, allows for the monitoring of the effects of production and constrains reservoir modelling, and can be achieved through the use of (freely available) satellite imagery.

We discuss the results of both techniques over two high enthalpy geothermal sites in Iceland: Reykjanes Peninsula and Torfajökull volcano. While the Reykjanes Peninsula has geothermal fields that have been producing for decades, Torfajökull's geothermal field, despite being the largest in Iceland, is not producing. For the subsurface characterization, we use S-wave velocity tomographic images derived from ambient noise seismic interferometry over the two geothermal sites. Within the tomographic images, low- and high-velocity anomalies are used to characterize subsurface structures, which complement current geological models with information at greater depths. From the monitoring point of view, radar satellite deformation measurements over both areas show displacements (subsidence) due to production (Reykjanes) and due to natural phenomena (Torfajökull). Finally, we summarize the lessons learnt and discuss outcomes on each technique.

1. INTRODUCTION

The key to minimizing the impact of geothermal production aftereffects, e.g. induced seismicity, subsidence, while maximizing the energetic potential is dependent on a good understanding of the subsurface and the driving mechanisms. This double objective (maximize production while minimizing the aftereffects) for production operations by data assimilation proved to be an excellent strategy for gas fields, e.g. [Chitu et al., 2017]. However, such studies rely on detailed knowledge of the static and dynamic processes of the subsurface, which is usually costly to obtain. Significant improvements in the cost, efficiency, methodologies and feasibility of geophysical measurements, together with data assimilation algorithms [Leeuwenburgh et al., 2011; Fokker et al, 2016; Zoccarato et al., 2016], boosted by the development of computational power and satellite technology have opened new perspectives in near-real-time monitoring [Spaans and Hooper, 2016].

High-resolution subsurface images can be achieved through active-source reflection seismics, but these techniques are expensive. Seismic tomography using earthquake-induced seismic waves as illumination provide substantial insights on both P and S-wave velocities but rely on the existence and optimal spatial distribution of earthquakes and precise S-waves first-arrival picks. Using Ambient Noise Tomography (ANT) with seismic interferometry (SI) does not require any active sources. It applies SI via time-domain cross-correlation in which new seismic responses between receivers are generated through the cross-correlation and summation of (noise) recordings from surrounding (noise) sources [Wapenaar, 2004]. Within the geothermal applications, ambient noise techniques have been used to characterize the subsurface S-wave velocity field and to understand the temporal evolution of the velocity models from field operations in producing fields. Amongst other examples, ambient noise has been explored in both sedimentary and magmatic environments such as Soultz-sous-Forêts [Calò and Dorbath, 2013a; Calò et al., 2013b], St. Gallen geothermal site in Switzerland [Obermann et al., 2015], Alsace in France [Lehujeur et al., 2015], and Iceland [Weemstra et al., 2016]; [Martins et al., 2019b], [Sanchez-Pastor et al., 2019].

Geodetic techniques significantly improved with the advent of space-based measurements. Global navigation satellite systems (GNSS), such as GPS, improved positioning capabilities, providing a unique way to measure surface deformation processes. Synthetic Aperture Radar (SAR) satellite sensors (e.g. ERS-1/2, ENVISAT, TerraSAR-X, RadarSat-1/2, Cosmo-Skymed, Sentinel-I, ALOS)

stimulated research and monitoring of Earth's surface deformation processes [Massonnet et al., 1998]. SAR sensors coupled to satellites became a unique tool to measure deformation over large areas now with a repeat time of 6 days. When compared with in situ levelling, the spatio-temporal resolution and coverage of SAR satellite missions, together with the reduction or elimination of fieldwork, are encouraging arguments to investigate InSAR (Interferometric Synthetic Aperture Radar) techniques further. Among other applications, InSAR is used to infer the size, shape, and depth of a volcano magma chamber through geophysical deformation modelling (e.g. [Mogi, 1958], [Okada, 1985], [Fukushima, 2005], [Segall, 2010]). In geothermal applications the monitoring of geothermal production through InSAR techniques is growing fast, mostly used in volcanic environments to associate production with volume change given modelled sources (e.g. [Jónsson, 1998], [Fialko and Simons, 2000], [Keiding, 2010], [Xu et al., 2017], [Parks et al., 2018], [Maghsoudi et al., 2018], [Bekesi et al., 2019a]) or to estimate fault parameters of induced seismicity after stress development and fault reactivation due to production (e.g. [Pedersen et al, 2003], [Jónsson et al., 2003], [Hole et al., 2007], [Takada and Furuya, 2010], [Yang et al., 2018], [Bekési et al., 2019b]).

This paper discusses the capabilities of both interferometric remote-sensing techniques, and provides constraints on their synergistic use to infer geothermal static and dynamic reservoir properties.

2. AREA OF INTEREST

We investigate the potential of both techniques over two volcanic-origin high-enthalpy geothermal sites in Iceland: Reykjanes Peninsula and Torfajökull volcano (Figure 1).

Iceland is an excellent location to test both techniques due to the high signal to noise ratio (SNR) achieved by the use of both radar and passive seismic interferometry. Except for snow cover periods, InSAR interferograms are usually highly coherent due to the low-density vegetation coverage and extensive coverage of rocks, which provides consistency in the backscattered signal between SAR acquisitions. Empirical Green's functions derived from ambient noise seismic interferometry are equally coherent, and the ambient noise sources arriving from the ocean in nearly every direction are highly energetic. Furthermore, existing geothermal production and deformation enable the association between each technique's capability and the production.

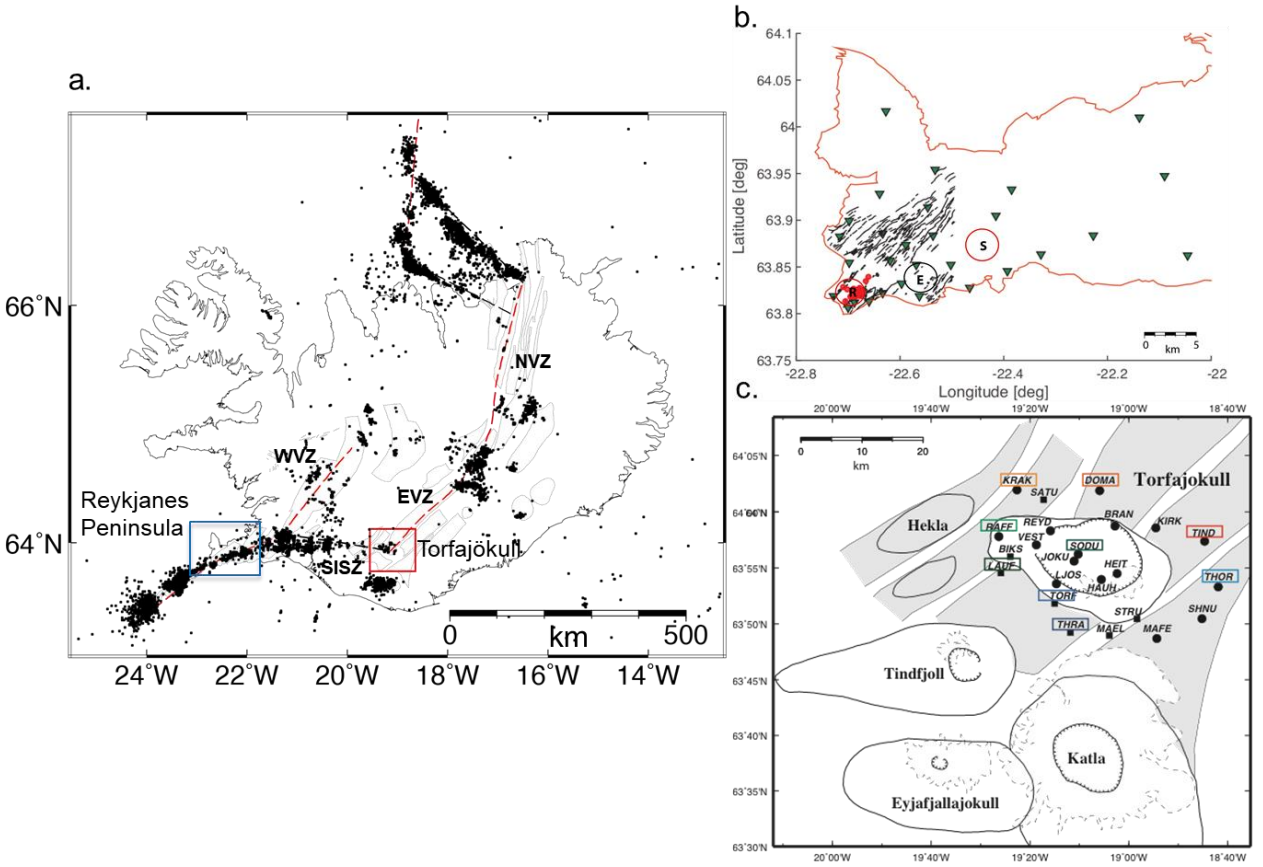

Figure 1: Map of Iceland and zooms of Reykjanes Peninsula and Torfajökull Volcano with corresponding seismicity (between 1995 and 2015 for indications of the seismic active areas). a) Iceland map with tectonic features: in light grey the volcanic systems (fissure swarms and central volcano or both) [Einarsson, 1987]; in red dashed line locate the plate boundary; black lines locate the transform fault systems; The nomenclatures NZV, EVZ and WVZ refer to North, East and West volcanic zones, respectively; SISZ refers to the location of the south Iceland seismic zone. b) West Reykjanes peninsula. Green triangles locate the onshore broadband stations developed under the EU-funded program Integrated Methods for Advanced Geothermal Exploration (IMAGE) for approximately 1.5 years [Martins et al., 2019b]. Black lines represent faults and fractures, and circles locate high-temperature areas from west to east, Reykjanes (R), Eldvörp (E), Svartsengi (S). c) Torfajökull seismic network and neighbouring volcanoes, where circles and squares locate the seismic network deployed in 2005 for about three months [Martins et al., 2019a]. Box in south-

central of map locates Torfajökull volcanic system at the intersection of the SISZ and EVZ, immediately north of Katla volcano.

The Reykjanes Peninsula, located at the southwestern tip of Iceland, has intense geothermal activities, which makes this geothermal field productive for decades (shallow and deep drilling). The field is producing and owes its source of heat to the MAR volcano-tectonic belt [Arnorsson et al., 1995]. During the IMAGE (Integrated Methods for Advanced Geothermal Exploration) project, an extensive seismic network was placed at and around Reykjanes Peninsula for nearly one and a half years in an attempt to exploit seismic imaging methodologies and capabilities for geothermal applications. The success of such seismic campaigns has been broadly reported (i.e., [Verdel et al., 2016]; [Weemstra et al., 2016]; [Darnet et al., 2018], [Toledo et al., 2018], [Blanck et al., 2019], [Martins et al., 2019b], [Sanchez-Pastor et al., 2019]), partly because of the availability of production data and existing induced seismicity and deformation.

Despite being the largest geothermal field in Iceland, Torfajökull's area is not subject to production. While the volcano has not erupted since 1477, it is one of the largest geothermal areas in Iceland with geothermal surface manifestations covering an area of 140 km^2. Some studies have been performed to understand Torfajökull's potential for geothermal exploitation (e.g. Ólafsson & Bjarnason [2000] and Palmason et al., [1970]). However, this area has also been suggested as a UNESCO World Heritage site for its unique geological features. The massive caldera (12x18 km) indicates the presence of a sizeable magma chamber, and is located in a unique tectonic setting at the intersection of a rift and a transform zone. The availability of both historical deformation data and a seismic campaign with a valuable network configuration for tomographic studies make this volcano ideal to assess the performance of both radar and seismic interferometric observations to understand the underlying subsurface.

2. METHODS

2.1 Geodetic Imaging

To estimate the deformation field over the whole SISZ (South Icelandic Seismic Zone, Figure 1), we processed the complete scenes of six ENVISAT tracks (three descending and three ascending modes) acquired between 2003 and 2010. The temporal distribution of the six tracks is shown in Fig. 2, where the observed interruption of acquisitions over the winter, due to snow cover, allows us to keep the coherence of the summer-to-summer acquisitions. The existence of six Envisat tracks over the same area is latitude dependent, which makes Iceland a privileged area as the six tracks constrain the estimation and decomposition of the surface displacement vectors due to the different acquisition geometries.

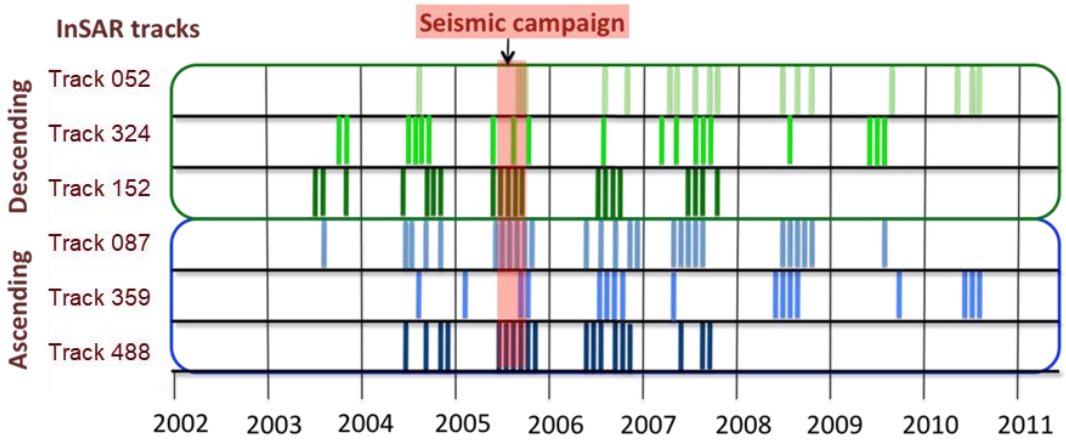

Figure 2: Time coverage of the available images of six ENVISAT tracks and time coverage of the 2005 seismic campaign (Fig. 1 c). Notice the gaps in winter acquisitions due to snow coverage.

We start by focusing the RAW images using the ROI_PAC software (Repeated Orbit Interferometric Package) [Schmidt, 2002], and process the interferograms using the Delft Object-oriented Radar Interferometric Software DORIS [Kampes et al., 2003]. For the time-series, we use the small-baseline approach of StaMPS (Stanford Method for Persistent Scatterers) and some of its software dependencies [Rosen et al., 2012, Foumelis et al., 2018, Werner et al., 2000, Bekaert et al., 2015a, b, Rosen et al., 2004]. We correct for the reference phase (flat-earth phase) and other geometric components of the interferometric phase such as topography and orbits by using a 25 m digital elevation model (DEM) from the National Land Survey of Iceland, and ESA DORIS orbits. We additionally apply a correction for the drift in the local oscillator frequency of ENVISAT satellite [Marinkovic and Larsen, 2015]. For the small baseline approach, we use a multilook of 5 in range and 4 in azimuth. To obtain the parameters of the source of deformation, we invert the estimated displacements of each track using a non-linear least-squares approach to solve for the parameters of a Yang magma source [Yang et al.,1988], a dipping prolate ellipsoid in an elastic half-space.

Here, we report on the processing of the deformation field over Torfajökull volcano. For the Reykjanes Peninsula we used the InSAR results derived by [Keiding et al., 2010] and [Parks et al., 2018] (see Discussion & Summary section).

2.3 Seismic Imaging

For the seismic imaging, we use the results of ANT described for both Torfajökull volcano and Reykjanes peninsula in [Martins et al., 2019a] and [Martins et al., 2019b], respectively. The distribution of both seismic networks is depicted in Fig. 1. The adopted procedure described in both publications follows the following summarized approach: 1. Division of the ambient noise recorded at two stations in portions of one hour. 2. Cross-correlation of the corresponding portions and summation of the correlated results

between all pairs of stations from which the surface-wave part of the Green's function is retrieved. 3. Tomographic inversion of the retrieved dispersion curves between pairs of stations. 4. Frequency-to-depth inversion to obtain the 3D S-wave velocity field.

3. RESULTS

3.1 Torfajökull's Surface Displacements and Seismic Tomography

Using InSAR time-series analysis as described above, we detect a linear displacement within Torfajökull caldera. We estimate the displacement velocities of each distributed backscattered point in time. We identify a pattern of subsidence beneath the SW part of the caldera. The detected deformation signal is on-going since at least the beginning of the time-series at the rates of up to ~13 mm/year (Fig 3). These results confirm those of Scheiber et al. [2011], but here, we use four extra satellite tracks and a longer time-series. We observe significant surface deformation in the NE corner of the studied area, but we limit our modelling to the Torfajökull region (area outlined in Fig. 1). The trend of the displacements in the NE-SW direction is from glacial isostatic adjustment (GIA) due to the melting of the biggest glacier in Iceland (Vatnajökull) and rebound of the earth's crust [Arnadottir et al., 2009], [Schmidt et al.,2012]. Another uplift signal can be identified in Fig. 3 in the SE-most corner, which is also due to crustal movements due to Iceland's shrinking ice caps mimicking a magma inflow signal at Katla volcano [Spaans et al., 2015]. A more detailed assessment on the separation of the superposition of deformation signals and on the best-fit source of displacements at depth after the joint inversion of the six tracks can be found in Martins et al. [2019c in prep].

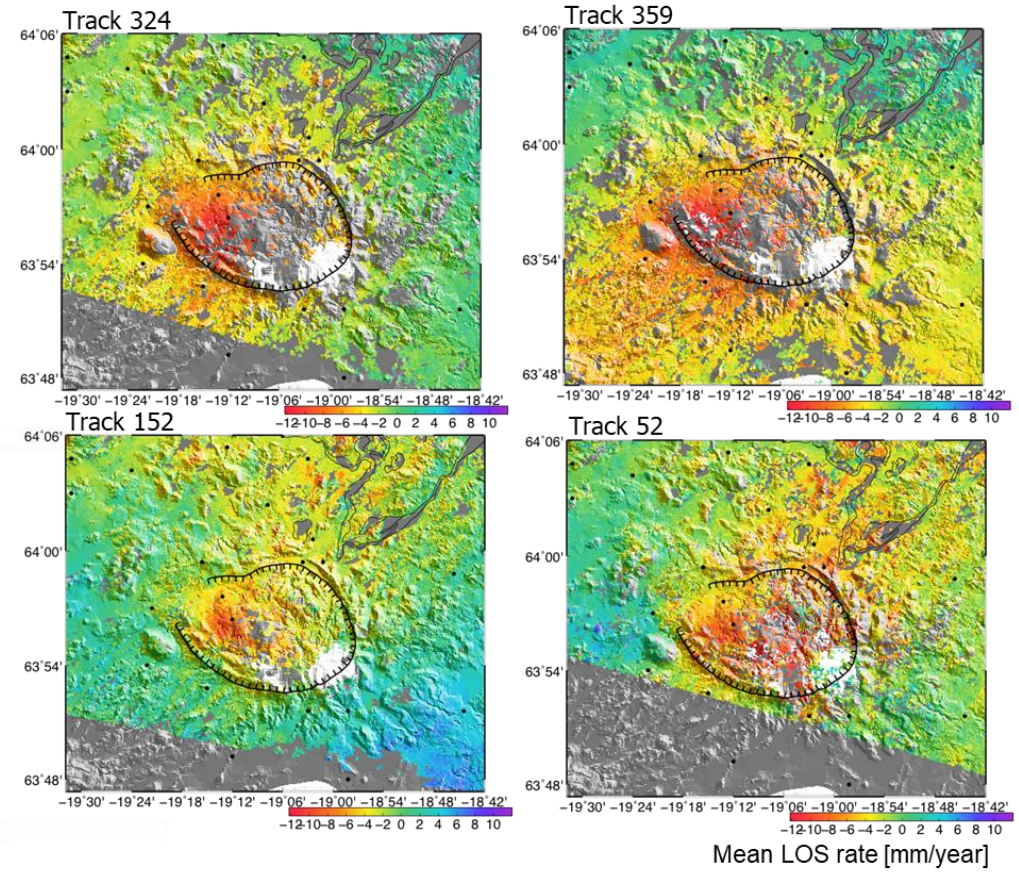

Figure 3: Estimated mean Line-of-Sight velocity of four out of the six processed tracks. The black line outlines the volcano caldera.

The estimated InSAR displacements can be fit with low residuals using a model of a NE-SW oriented spheroidal body at ~5 km depth, undergoing a pressure decrease that is uniform in space and time. The best-estimate source of displacements is an ellipsoidal source starting at ~5 km depth, sized 4.5 x 5 km.

Fig. 4 depicts an example of the modelled source for Track 324, with a preferential NW-SE orientation and located at the southern area within the volcano caldera. The residuals indicate that most of the estimated deformation signal can be explained by the modelled source. However, a residual uplift or horizontal (moving westward) signal is left on the west side in opposition to a residual subsidence or horizontal (moving eastwards) signal in the east side of the modelled area, signaling a possible contribution of other superimposed source of deformation. A horizontal component of displacement that may be associated with tectonic spreading, or the vertical displacement associated with GIA, or both, may explain the observed residuals.

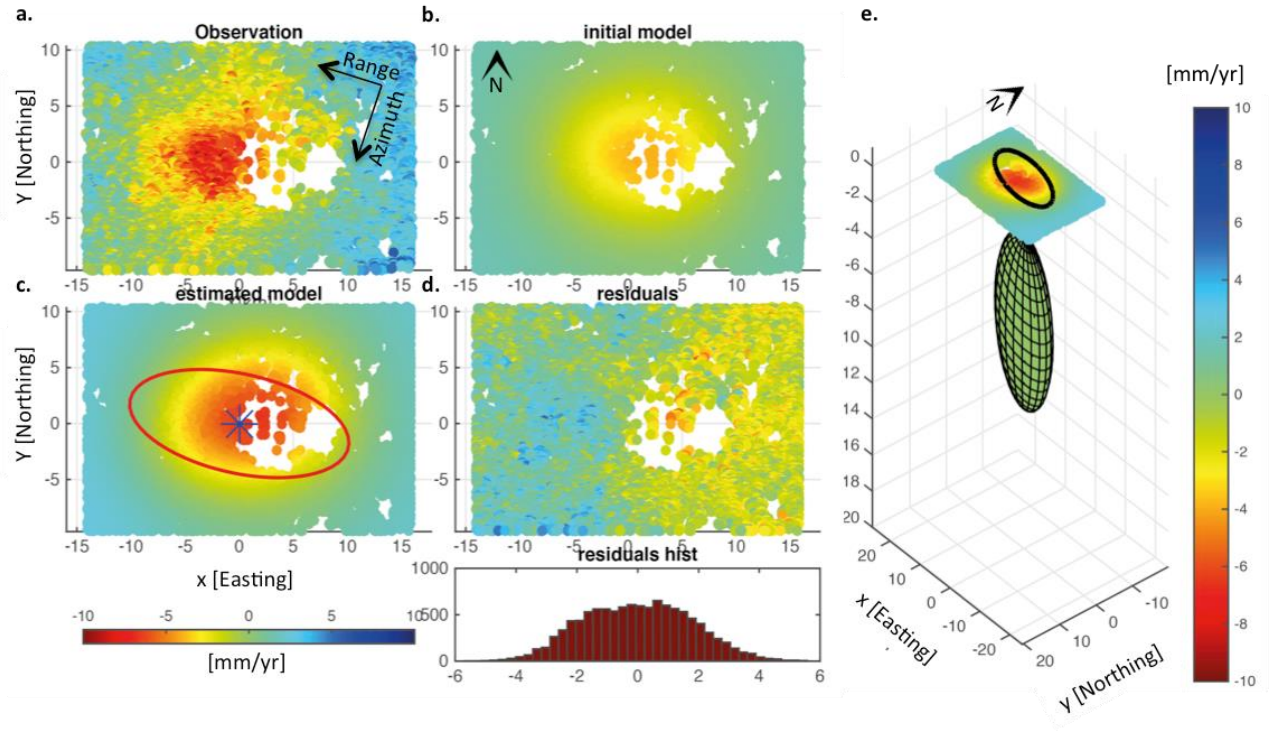

Figure 4: Modelling of the estimated displacements of Track 324 (a) with the corresponding initial model, final model and residuals (b, c, and d). In e) we show the estimated prolate spheroid in a 3D view.

From the results of the seismic ANT [Martins et al., 2019a] we do not detect any anomaly below -10% of velocity variations from the mean velocity at the location of the subsidence signal. Fig 5 shows the ANT results displayed in a 3D model with vertical axis exaggerated for visualization purposes. As expected for a magma chamber with molten or partially molten rock, a low-velocity anomaly is detected. The anomalies vary between 7 to 15 % (high-velocity anomalies) and -7 to -15 % (low-velocity anomalies), displayed in blue and orange, respectively. The area where we observe and modelled the subsidence is situated between the three detected main low-velocity anomalies from ANT in south, southeast, and southwest located outside the volcano caldera and below 3 km depth. Within the volcano caldera and at the location of the modelled source of subsidence, we do not detect any abnormally low- or high-velocity anomaly.

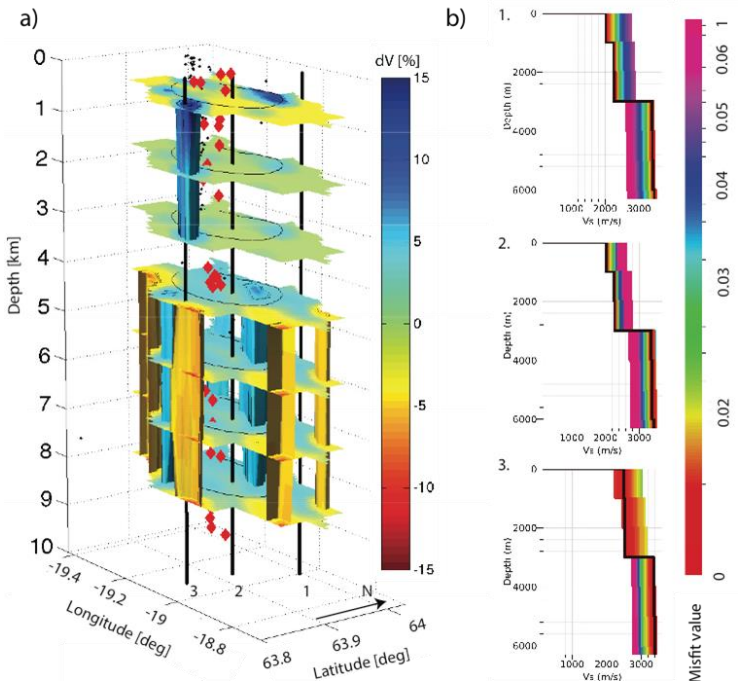

Figure 5. a) 3-D shear velocity model with reference to a 1-D velocity model at depth after Martins et al., [2019a]. The vertical axis is exaggerated for visualization purposes. The circular-shaped black line represents the caldera outline at the surface. Black dots represent high-frequency earthquakes and red diamonds low-frequency earthquakes relocated by [Lippitsch et al., 2005]. Black vertical lines represent the centre of the grid cells of the profiles at b). b) Depth velocity

of the ~30000 models with the corresponding misfit. 1, 2 and 3 show examples of the inversion models for grid cells at the edges and centre of the modelled space. The black line represents the model with the minimum misfit.

3.2 Reykjanes Peninsula

For the seismic imaging, we focus on the higher resolution results of ANT [Martins et al., 2019b] and interpret 3D S-wave velocity cross-sections for 1 km resolution to have enough ray-path coverage over the Reykjanes geothermal field. We use the 3D- S-wave velocity field with 1 km resolution results under the strong assumption that the straight-ray approximation holds for the retrieved surface-waves. While the assumption of direct propagation between stations holds for homogeneous media, it may not hold for extreme velocity variations where the waves may suffer refraction. The practical reason to assume that the direct wave propagation still holds for 1 km resolution is to have enough coverage over the Reykjanes geothermal field and to be able to draw possible applications of the methodology over a more studied geothermal field. However, while the authors were conservative in not interpreting the 1 km results for the above-mentioned reasons, the derived results in the publication shows a good spatial correspondence of the velocity anomalies between 1 km and 3 km resolution.

The 1 km resolution S-wave velocity model is presented in Figure 6 with the corresponding identified cross-sections. In Figure 6a, the observed local low-velocity anomalies at the Reykjanes geothermal field match the location of the intensively exploited part of the geothermal reservoir. Such spatial correspondence may indicate that the observed low-velocity anomalies might be related to a heat source, water inclusion, or both [O'Connell et al., 1974, Mavko 1980]. The cross-sections displayed in Fig. 6 (a1 to a3) show the 3D S-wave velocities at the Reykjanes geothermal field from 1 to 6 km depth of the highly explored area. The cross-sections from b1 to b2 cross the Eldvorp (E) geothermal field and b3 to b4 the Svartsengi (S) geothermal field. The cross-sections numbered from c1 to c2 cross the three geothermal fields in the SW-NE direction and c1 only the Reykjanes geothermal field (R). For all the displayed cross-sections, we observe velocities lower than those of outside the locations of surface geothermal manifestations. Note that immediately outside the central area of geothermal exploration (Fig.6 a4), the detected low-velocity anomalies are not present anymore, possibly indicating a colder system.

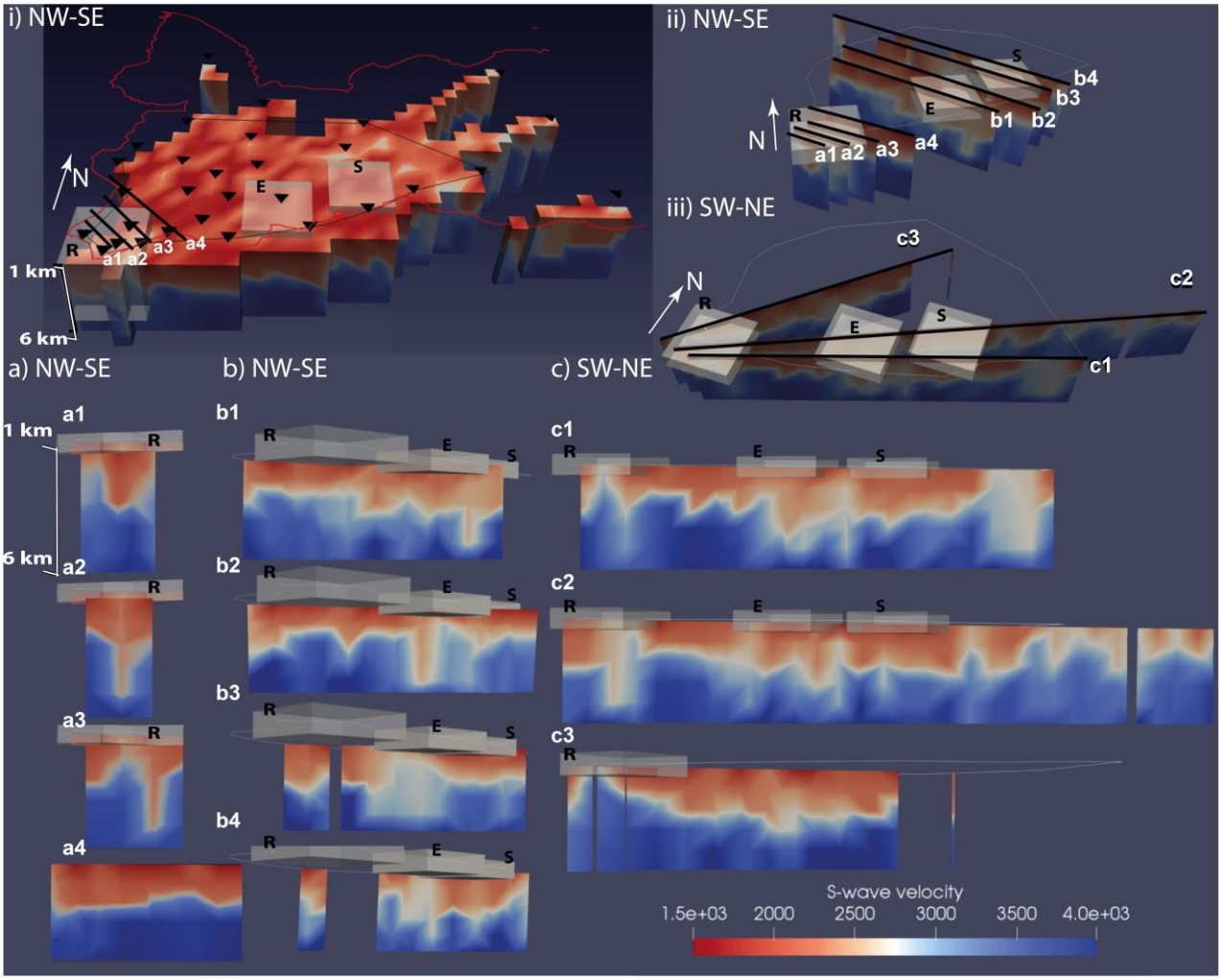

Figure 6: 3D S-wave velocity field and corresponding identified cross-sections between 1 and 6 km depth. The model has 1 km spatial resolution and 1 km depth resolution. i) General view of the 3D S-wave velocity model extension. The red line delimits the WRP coastal outline, with an inner previously defined polygon also in red. Black triangles indicate the on-shore broadband station locations and the black lines the cross-sections displayed in a). The cubes denote the high-temperature areas (mapped by ISOR) from west to east, the Reykjanes (R), Eldvorp (E), Svartsengi (S) geothermal fields. ii) The NW-SE location of the cross-sections displayed in a) and b) and the location of the geothermal fields. iii) The SW-NE location of the cross-sections displayed in c). a, b and c, show the cross-sections identified in i, ii and iii and also display the geothermal field whenever the cross-section crosses the geothermal field location.

For the geodetic imaging, we did not perform any processing, but focused our interpretation on existing studies using geodetic data (levelling, GPS and InSAR) to infer geothermal reservoir processes from Keiding et al., [2010], Parks et al., [2018], and Receveur et al., [2019]. Surface displacements in the area of Reykjanes geothermal field estimated from Envisat SAR data show surface subsidence up to 10 cm that correlates with the beginning of production in the field in May 2006 [Keiding et al., 2010]. Parks et al., [2018], used Envisat, TerraSAR-X and GNSS data to estimate the cumulative ground displacements between 2003 and 2016. The estimated location of the contracting sources and depths correlate well with the low-velocity cavity imaged by ANT. The same holds for the results of Receveur et al., [2019] using more recent deformation data from Sentinel-1 satellite.

DISCUSSION AND SUMMARY

While the Earth's surface inflates or deflates as a result of tensile or compressive internal forces (stress) in the subsurface, geodetic measurements are used to quantify the amount of deformation (strain) at the surface. Surface displacements in geothermal areas can be a result of coupling processes like flow, pressure build-up/release during pore volume increase/reduction, reservoir cooling, or in case there is no production, natural processes such as contracting due to cooling, regional extension, crystallization, expansion due to gas exsolution, and ongoing hydrothermal activity. If, on the one hand, these are time-dependent processes that can be modelled dynamically (dynamic model), surface displacements can also be used to solve for subsurface characterization (e.g. fault plane solutions or magma reservoir) through geodetic imaging (static model).

As seismic waves travel through the Earth's interior, they can be accelerated or decelerated depending on the different materials encountered along the seismic propagation path. With respect to a reference velocity model as a function of depth, it is possible to estimate velocity anomalies and distinguish different subsurface structures (static model) by seismic imaging. Other ambient noise seismic interferometric methodologies can also identify temporal changes in the wave propagation due to processes in the subsurface, namely geothermal production.

The results underline the potential of individual and integrated knowledge derived from both seismic and geodetic imaging. These techniques can help to constrain geomechanics, fluid flow and heat transport parameters through expansion/contraction of reservoirs and wavefield propagation changes. Parameters like temperature, density, fluid location, structural geological mapping, pressure, as well as on the volcanic geological history and hazard assessment, can also be constrained with the explored measurements. In table 1, we summarize some of the most relevant characteristics of both described techniques. Note that in this study, we focus only on the generation of geodetic or seismic imaging products and the same holds for the parameters described in Table 1. However, both datasets (‘Input data’ in Table 1) can be processed in different manners to access other subsurface processes such as fault solutions after induced seismicity events modelled from single interferograms using InSAR, or temporal changes due to production from coda waves. Additionally, for both case study applications, seismic images of shallower depths would be preferred for a possible confrontation with production data. For this, the use of higher recorded frequencies of ambient noise or a combination of group and phase velocity picks and further inversion from frequency to depth would allow a more comprehensive knowledge of the shallow subsurface.

Table 1. Some relevant parameters between the results of geodetic (InSAR based) and seismic (ANT based) imaging.

	Geodetic imaging (InSAR based)	**Seismic Imaging (ANT based)**
Input Data	Satellite SAR images: RAW (level-0) or SLC (Single Look Complex images)	Network of seismometers: Vertical or/and horizontal (for anisotropy studies) component of displacements.
Intermediate and final products	Surface deformation, surface morphology and reflectivity	Retrieval of surface waves from seismic interferometry. Azimuthal velocity variations, S-wave velocity field, S-wave velocity anomalies
Spatial Coverage	Scene size (ground footprint) depending on the satellite: 20 x 20 km or up to 250 km swath (length along a track)	Dependent on the station-network configuration and interstation distances. Can be applied for local, regional or global networks.
Temporal coverage	Dependent on satellite sensor and location on Earth surface. Earliest in 1991 (ERS-1/2) up to current date (Sentinel-1)	Dependent on availability of seismic data
Temporal sampling	Depending on satellite revisiting time and desired resolution. With Sentinel-1 it is possible up to 6.days. Future satellites (e.g. CubeSats) may provide an even higher temporal sampling.	Dependent on the type of seismic instrument, only applicable for tomography if tomographic inversion is performed using different temporal seismic acquisitions
Spatial resolution	1 to 20 m	Dependent on the station-network configuration and interstation distances.

Sensitivity at depth	Dependent on the radius-to-depth source ratio	Dependent on the bandwidth, interstation distance and sensitivity kernels.
Main error sources	Phase unwrapping especially in areas of low coherence, variation in atmospheric properties, topography, orbital errors.	Limited ambient noise (source) energy, limited number of stations, non-uniform source distribution, presence of multiple surface wave modes, wrong phase/group velocity picks.
Final and Intermediate products	Final (per point): Rate of displacements Intermediate (per point): Coherence, surface deformation per point at each acquisition time, amplitude, height	Final: 3D S-wave velocity field, S-wave velocity anomalies Intermediate: Empirical Green's functions, Ballistic Surface waves, azimuthal velocity estimation, time-dependent
Advantages over similar techniques	Cost-effective, large area coverage, of centimetric to millimetric levels of accuracy, depending on the AOI possible to go back to 1992 deformation measurements, measurements regardless weather conditions, no fieldwork requires	Possible to recover past seismic acquisitions, no need for active sources or earthquakes therefore economical.
Limitations	Loss of coherence between acquisitions, line of sight of the satellite measurements only, not sensitive to north-south oriented surface deformation.	3D S-wave velocity derived but not P-wave, long acquisition periods are required.
Applications	Reservoir pressure change estimation (with the corresponding spatial extent), monitoring of production after effects (e.g. subsidence), locating structures controlling the geothermal fluid movement (e.g. faults, calderas, basement and lateral permeability controls)	Locating heat sources, complementary to understanding MT results, general subsurface characterization (lithological variations with depth), the estimated S-wave velocity field can be used to constrain induced event location.

Geodetic imaging over Torfajokull reveals a contracting source located at approximately 5 km depth and with a size of 4.5 by 5km within the volcano caldera. In the presence of a molten magma reservoir, the estimated seismic image would "see" low-velocity anomalies at the location of the estimated source by inversion of InSAR LOS velocities. This is not what is observed. Instead, low-velocities are located in the southeast, southwest, and south, outside the volcano caldera. The contracting source could possibly be due to the cooling down of pre-existent molten material.

The seismic imaging over Reykjanes peninsula, while it covers a broader area, reveals more nuances. The cross-sections displayed in Fig. 6 (a1 to a3) show the 3D S-wave velocities at the Reykjanes geothermal field from 1 to 6 km depth of the highly explored area. At this location, it is possible to identify a low-velocity cavity extended in the SW-NE direction reaching the resolution depth. The same site is described by [Friðleifsson et al., 2018a] as the area of up-flow targeted by IDDP-2 is interpreted as hotter and more permeable. A resistivity model based on a 3D inversion of MT data indicates that the IDDP-02 well was drilled into a low resistivity anomaly, which coincides remarkably well with the observed low S-wave velocities in Fig. 6 a1 and a2. In this Figure, we plot the cross-sections at the approximate locations of the cross-sections in [Karlsdóttir et al., 2018]. The centre of the three NE-SW cross-sections (a1, a2 and a3) is close to the location of the wells RN-17, RN-10, and IDDP-02 from west to east, respectively. However, the interpretation is not straightforward, as resistivity is one of the most variable physical properties of rocks [Ussher et al., 2000]. In the case of the SW tip of Reykjanes Peninsula, low resistivities can be correlated with clay hydrothermal alteration, water-rock interaction, and chemical transport by the geothermal fluids [Karlsdóttir et al., 2018]. Whenever there are more conductive clays with high water content (e.g. smectite), which often occurs at specific temperature regimes, the seismic waves will propagate with lower speeds [Ussher et al., 2000]. Well-log measurements could help to constrain the interpretation and a more detailed comparison like the one of [Karlsdóttir, et al., 2018]. A comparison between the log results and the S-wave velocity field would be of added value.

The low S-wave velocity anomaly extends for 2 km from the location of cross-section a1 until a3 in the SW-NE (Fig. 6) the same place of the high fault density with fractures striking between 0º and 20º and between 41º and 60º [Clifton at al.,2006]. If the detected low velocity cavity structure is partially a result of fracturing between the cross-sections a1 and a2 the preferred direction is ~30º from the north and between a2 and a3 changes to 60º The estimated high temperatures and geological setting suggest that the cold water flowing down through the highly permeable detected fractures meets with the up-flow of warmer water and enhancing the geothermal potential. Regarding temperatures in the well RN-10 (located at the surface of the profile a2 in Fig.6), temperature logs are reported to have the higher temperatures (320 degrees Celsius) in the reservoir (below 1000 m depth) a convective flow below that depth [Franzson et al., 2002]. Well IDDP-02 deviates horizontally at 3000 km depth towards the direction of the cross-section of the well RN-10 that reaches ~ 4500 vertical depth [Friðleifsson et al., 2018a]. The same authors report on an estimated bottom hole temperature of 535 degrees Celsius and the total loss of circulation below 3000 m up to the final IDDP-02 drilling depth, which indicates that hotter environments may be reached.

ACKNOWLEDGEMENTS

The Envisat images were acquired by the European Space Agency (ESA). The results in this article received partial funding from the EC Seventh Framework Programme under the grant agreement No. 608553 (Project IMAGE), from the FP7 Environment Programme of the European Comission No. 308377 (FULTUREVOLC), and from the Portuguese Foundation for Science and Technology (FCT-DFRH-SFRH/BD/61663/2009).

REFERENCES

Blanck, H., P. Jousset, G. P. Hersir, K. Ágústsson and Ó. G. Flóvenz (2019). "Analysis of 2014–2015 on-and off-shore passive seismic data on the Reykjanes Peninsula, SW Iceland." Journal of Volcanology and Geothermal Research.

Calò, M. and C. Dorbath (2013). "Different behaviours of the seismic velocity field at Soultz-sous-Forêts revealed by 4-D seismic tomography: case study of GPK3 and GPK2 injection tests." Geophysical Journal International 194(2): 1119-1137.

Calò, M., X. Kinnaert and C. Dorbath (2013). "Procedure to construct three-dimensional models of geothermal areas using seismic noise cross-correlations: application to the Soultz-sous-Forêts enhanced geothermal site." Geophysical Journal International 194(3): 1893-1899.

Chitu, A., O. Leeuwenburgh, T. Candela, S. Osinga, D. Kraaijpoel and B. Wassing (2017). Optimizing of operational strategies in producting gas fields mitigating induced seismic risk.

Clifton, A. E. and S. A. Kattenhorn (2006). "Structural architecture of a highly oblique divergent plate boundary segment." Tectonophysics 419(1-4): 27-40.

Darnet, M., N. Coppo, P. Wawrzyniak, S. Nielsson, G. Fridleifsson and E. Schill (2019). "Imaging and monitoring the Reykjanes supercritical geothermal reservoir in Iceland with time-lapse CSEM and MT measurements." arXiv preprint arXiv:1905.07899.

Fialko, Y. and M. Simons (2000). "Deformation and seismicity in the Coso geothermal area, Inyo County, California: Observations and modeling using satellite radar interferometry." Journal of Geophysical Research: Solid Earth 105(B9): 21781-21793.

Fokker, P. A., B. B. T. Wassing, F. J. Van Leijen, R. F. Hanssen and D. A. Nieuwland (2016). "Application of an ensemble smoother with multiple data assimilation to the Bergermeer gas field, using PS-InSAR." Geomechanics for Energy and the Environment 5: 16-28.

Foumelis, M. (2018). "Vector-based approach for combining ascending and descending persistent scatterers interferometric point measurements." Geocarto international 33(1): 38-52.

Franzson, H., S. Thordarson, G. Björnsson, S. T. Gudlaugsson, B. Richter, G. O. Fridleifsson and S. Thorhallsson Reykjanes high-temperature field, SW-Iceland. Geology and hydrothermal alteration of well RN-10. Workshop on Geothermal Reservoir Engineering.

Friðleifsson, G. Ó., W. A. Elders, R. A. Zierenberg, A. P. G. Fowler, T. B. Weisenberger, K. G. Mesfin, Ó. Sigurðsson, S. Níelsson, G. Einarsson, F. Óskarsson and others (2018). "The Iceland Deep Drilling Project at Reykjanes: Drilling into the root zone of a black smoker analog." Journal of Volcanology and Geothermal Research.

Fukushima, Y., V. Cayol and P. Durand (2005). "Finding realistic dike models from interferometric synthetic aperture radar data: The February 2000 eruption at Piton de la Fournaise." Journal of Geophysical Research: Solid Earth 110(B3).

Hole, J., C. Bromley, N. Stevens and G. Wadge (2007). "Subsidence in the geothermal fields of the Taupo Volcanic Zone, New Zealand from 1996 to 2005 measured by InSAR." Journal of Volcanology and Geothermal Research 166(3-4): 125-146.

Jónsson, S., P. Segall, R. Pedersen and G. Björnsson (2003). "Post-earthquake ground movements correlated to pore-pressure transients." Nature 424(6945): 179.

Kampes, B. M., R. F. Hanssen and Z. Perski (2003). Radar interferometry with public domain tools. Proceedings of FRINGE.

Karlsdóttir, R., A. M. Vilhjálmsson and E. Á. Guðnason (2018). "Three dimensional inversion of magnetotelluric (MT) resistivity data from Reykjanes high temperature field in SW Iceland." Journal of Volcanology and Geothermal Research.

Keiding, M., T. Árnadóttir, S. Jonsson, J. Decriem and A. Hooper (2010). "Plate boundary deformation and man-made subsidence around geothermal fields on the Reykjanes Peninsula, Iceland." Journal of Volcanology and Geothermal Research 194(4): 139-149.

Keiding, M., T. Árnadóttir, E. Sturkell, H. Geirsson and B. Lund (2008). "Strain accumulation along an oblique plate boundary: the Reykjanes Peninsula, southwest Iceland." Geophysical Journal International 172(2): 861-872.

Kiyoo, M. (1958). "Relations between the eruptions of various volcanoes and the deformations of the ground surfaces around them." Earthq Res Inst 36: 99-134.

Leeuwenburgh, O., J. Brouwer and M. Trani (2011). "Ensemble-based conditioning of reservoir models to seismic data." Computational Geosciences 15(2): 359-378.

Lehujeur, M., J. Vergne, J. Schmittbuhl and A. Maggi (2015). "Characterization of ambient seismic noise near a deep geothermal reservoir and implications for interferometric methods: a case study in northern Alsace, France." Geothermal Energy 3(1): 3.

Lippitsch, R., R. S. White and H. Soosalu (2005). "Precise hypocentre relocation of microearthquakes in a high-temperature geothermal field: the Torfajökull central volcano, Iceland." Geophysical Journal International 160(1): 370-387.

Maghsoudi, Y., F. van der Meer, C. Hecker, D. Perissin and A. Saepuloh (2018). "Using PS-InSAR to detect surface deformation in geothermal areas of West Java in Indonesia." International journal of applied earth observation and geoinformation 64: 386-396.

Marinkovic, P. and Y. Larsen (2015). On resolving the local oscillator drift induced phase ramps in ASAR and ERS1/2 interferometric data–the final solution. Proceedings of the 9th international workshop Fringe.

Martins, J., E. Ruigrok, D. Draganov, A. Hooper, R. Hanssen, R. White and H. Soosalu (2019a). "Imaging Torfajökull's magmatic plumbing system with seismic interferometry and phase velocity surface wave tomography." Journal of Geophysical Research: Solid Earth 124(3): 2920-2940.

Martins, J. E., Weemstra, C., Ruigrok, E., Verdel, A., Jousset, P., Hersir, G.P. (2019b). " 3D S-wave velocity imaging of the Reykjanes peninsula high-enthalpy geothermal fields with ambient-noise tomography." Journal of Volcanology and Geothermal Research, [in Press].

Martins, J. E., Hooper, A., Samiei-Esfahani, S., Hanssen, R. F., (2019c), “The magmatic plumbing system of Torfajökull volcano from geodetic and seismic imaging”. [in prep]

Massonnet, D. and K. L. Feigl (1998). "Radar interferometry and its application to changes in the Earth's surface." Reviews of Geophysics 36(4): 441-500.

Mavko, G. M. (1980). "Velocity and attenuation in partially molten rocks." Journal of Geophysical Research: Solid Earth 85(B10): 5173-5189.

Obermann, A., T. Kraft, E. Larose and S. Wiemer (2015). "Potential of ambient seismic noise techniques to monitor the St. Gallen geothermal site (Switzerland)." Journal of Geophysical Research: Solid Earth 120(6): 4301-4316.

O'Connell, R. J. and B. Budiansky (1974). "Seismic velocities in dry and saturated cracked solids." Journal of Geophysical Research 79(35): 5412-5426.

Okada, Y. (1985). "Surface deformation due to shear and tensile faults in a half-space." Bulletin of the Seismological Society of America 75(4): 1135-1154.

Ólafsson, M. and J. Ö. Bjarnason (2000). Chemistry of fumarole and hot springs in the Torfajökull geothermal area, South Iceland. Proceedings World Geothermal Congress, Kyushu-Tohoku Japan.

Palmason, G., J. Friedman, R. Williams Jr, J. Jonsson and K. Saemundsson (1970). "Aerial infrared surveys of Reykjanes and Torfajökull thermal areas, Oceland, with a section on cost of exploration surveys." Geothermics 2: 399-412.

Parks, M., F. Sigmundsson, Ó. Sigurðsson, A. Hooper, S. Hreinsdóttir, B. Ófeigsson and K. Michalczewska (2018). "Deformation due to geothermal exploitation at Reykjanes, Iceland." Journal of Volcanology and Geothermal Research.

Pedersen, R., S. Jónsson, T. Árnadóttir, F. Sigmundsson and K. L. Feigl (2003). "Fault slip distribution of two June 2000 MW6. 5 earthquakes in South Iceland estimated from joint inversion of InSAR and GPS measurements." Earth and Planetary Science Letters 213(3-4): 487-502.

Receveur, M., F. Sigmundsson, V. Drouin and M. Parks (2018). "Ground deformation due to steam cap processes at Reykjanes, SW-Iceland: effects of geothermal exploitation inferred from interferometric analysis of Sentinel-1 images 2015–2017." Geophysical Journal International 216(3): 2183-2212.

Rosen, P. A., E. Gurrola, G. F. Sacco and H. Zebker (2012). The InSAR scientific computing environment. EUSAR 2012; 9th European Conference on Synthetic Aperture Radar, VDE.

Rosen, P. A., S. Hensley, G. Peltzer and M. Simons (2004). "Updated repeat orbit interferometry package released." Eos, Transactions American Geophysical Union 85(5): 47-47.

Sánchez-Pastor, P., A. Obermann, M. Schimmel, C. Weemstra, A. Verdel and P. Jousset (2019). "Short-and long-term variations in the Reykjanes geothermal reservoir from seismic noise interferometry." Geophysical research letters.

Scheiber-Enslin, S. E., P. C. LaFemina, E. Sturkell, A. J. Hooper and S. J. Webb (2011). "Geodetic investigation of plate spreading along a propagating ridge: the Eastern Volcanic Zone, Iceland." Geophysical Journal International 187(3): 1175-1194.

Schmidt, D. A. (2002). The Kindematics of Faults in the San Francisco Bay Area Inferred from Geodetic and Seismic Data, University of California, Berkeley.

Schmidt, P., B. o. Lund, rn, T. Arnadottir and H. Schmeling (2012). "Glacial isostatic adjustment constrains dehydration stiffening beneath Iceland." Earth and Planetary Science Letters 359: 152-161.

Segall, P. (2010). Earthquake and volcano deformation, Princeton University Press.

Spaans, K. and A. Hooper (2016). "InSAR processing for volcano monitoring and other near-real time applications." Journal of Geophysical Research: Solid Earth 121(4): 2947-2960.

Spaans, K., t. Hreinsd\'o, Sigr\'u,n, A. Hooper and f. \'O, Benedikt Gunnar (2015). "Crustal movements due to Iceland’s shrinking ice caps mimic magma inflow signal at Katla volcano." Scientific reports 5: 10285.

Takada, Y. and M. Furuya (2010). "Aseismic slip during the 1996 earthquake swarm in and around the Onikobe geothermal area, NE Japan." Earth and Planetary Science Letters 290(3-4): 302-310.

Ussher, G., C. Harvey, R. Johnstone and E. Anderson Understanding the resistivities observed in geothermal systems. Proceedings World Geothermal Congress.

Verdel, A., H. Wedemeijer, B. Paap, V. Vandeweijer, C. Weemstra, P. Jousset, S. Franke, H. Blanck, g. \'A, Kristj\'a,n and G. P. a. Hersir, ll (2016). Reykjanes ambient noise reflection interferometry. {Proc. European Geothermal Congress, Strasbourg, France}.

Wapenaar, K. (2004). "Retrieving the elastodynamic Green's function of an arbitrary inhomogeneous medium by cross correlation." Physical review letters 93(25): 254301.

Weemstra, C., A. Obermann, A. Verdel, B. Paap, H. Blanck, E. Gunason, G. P. Hersir, P. Jousset and Ó. Sigurdsson (2016). Time-lapse seismic imaging of the Reykjanes geothermal reservoir. Proc. European Geothermal Congress, Strasbourg, France.

Werner, C., U. Wegmüller, T. Strozzi and A. Wiesmann (2002). Processing strategies for phase unwrapping for INSAR applications. Proceedings of the European Conference on Synthetic Aperture Radar (EUSAR 2002).

Xu, X., D. T. Sandwell, E. Tymofyeyeva, A. González-Ortega and X. Tong (2017). "Tectonic and anthropogenic deformation at the Cerro Prieto geothermal step-over revealed by Sentinel-1A InSAR." IEEE Transactions on Geoscience and Remote Sensing 55(9): 5284-5292.

Yang, Y. H., M. C. Tsai, J. C. Hu, M. A. Aurelio, M. Hashimoto, J. A. P. Escudero, Z. Su and Q. Chen (2018). "Coseismic slip deficit of the 2017 Mw 6.5 Ormoc earthquake that occurred along a creeping segment and geothermal field of the Philippine fault." Geophysical research letters 45(6): 2659-2668.

Zoccarato, C., Ba\`u, D., M. Ferronato, G. Gambolati, A. Alzraiee and P. Teatini (2016). "Data assimilation of surface displacements to improve geomechanical parameters of gas storage reservoirs." Journal of Geophysical Research: Solid Earth 121(3): 1441-1461.